Highlights of Joint Research

Supercomputer Center

The Supercomputer Center (SCC) is a part of the Materials Design and Characterization Laboratory (MDCL) of ISSP. Its mission is to serve the whole community of computational condensed-matter physics of Japan providing it with high performance computing environment. In particular, the SCC selectively promotes and supports large-scale computations. For this purpose, the SCC invites proposals for supercomputer-aided research projects and hosts the Steering Committee, as mentioned below, that evaluates the proposals.

The ISSP supercomputer system consists of two subsystems: System A, which is intended for a parallel computation with relatively smaller number of nodes connected tightly, and System B, which is intended for more nodes with relatively loose connections. In July, 2010, the SCC replaced the two supercomputer subsystems. The current system B is SGI Altix ICE 8400EX, which consists of 30 racks or 15360 cores whereas the system A is NEC SX-9, which consists of 4 nodes or 64 cpus. They have in total 200 TFlops.

The hardware administration is not the only function of the SCC. The ISSP started hosting Computational Materials Science Initiative (CMSI), a new activity of promoting materials science study with next-generation parallel supercomputing. This activity is financially supported by the MEXT HPCI strategic program. In CMSI, a number of major Japanese research institutes in various branches of materials science are involved. The SCC supports the activities of CMSI as its major mission.

System C - FUJITSU PRIMEHPC FX10 has just been installed in April, 2013. It is highly compatible with K computer, the largest supercomputer in Japan. System C consists of 384 nodes, and each node has 1 SPARC64^{TM} IXfx CPU (16 cores) and 32 GB of memory. The total system achieves 90.8 TFlops theoretical peak performance.

Class	Max/Min Points	Application	Number of Projects	Total Points			
				Applied		Approved	
				System A	System B	System A	System B
A	<100	any time	3	10	290	10	290
B	<2k	twice a year	49	14.5k	40.8k	14.1k	29.5k
C	<20k	twice a year	121	448.8k	919.4k	422.3k	406.5k
D	<20k	any time	11	0	94.0k	0	53.0k
E	<30k	twice a year	21	-	597.0k	-	286.0k
S	>10k	twice a year	0	0	0	0	0
CMSI				-	-	-	151.6k
Total			205	463.3k	1,651.5k	436.4k	926.9k

Table 1. Research projects approved in 2012
The maximum points allotted to the project of each class are the sum of the points for the two systems; Computation for 1 CPU•hour corresponds to 0.6 and 0.02 points for System-A and System-B, respectively.

All staff members of universities or public research institutes in Japan are invited to propose research projects (called User Program). The proposals are evaluated by the Steering Committee of SCC. Pre-reviewing is done by the Supercomputer Project Advisory Committee. In school year 2012 totally 205 projects were approved. The total points applied and approved are listed on Table 1 below.

The research projects are roughly classified into the following three (the number of projects approved):

First-Principles Calculation of Materials Properties (94)
Strongly Correlated Quantum Systems (53)
Cooperative Phenomena in Complex, Macroscopic Systems (58)

Projects in all three categories involve both methodology of computation and its applications. The results of the projects are reported in 'Activity Report 2012' of the SCC. Every year 3-4 projects are selected for “invited papers” and published at the beginning of the Activity Report. In the Activity Report 2012, the following three invited papers are included:

"First-Principles X-ray Photoelectron Spectroscopy Calculation on Defects in Semiconductors",
Jun TAMAUCHI, Yoshihide YOSHIMOTO, and Yuji SUWA
"Topological Hall Effect in Spatially Inhomogeneous Systems",
Masafumi UDAGAWA
"Huge-Scale Molecular Study of Multi-Bubble Nuclei",
Hiroshi WATANABE and Nobuyasu ITO

Neutron Science Laboratory

The Neutron Science Laboratory (NSL) has been playing a central role in neutron scattering activities in Japan since 1961 by performing its own research programs as well as providing a strong General User Program with the university-owned various neutron scattering spectrometers installed at the JRR-3 (20MW) operated by Japan Atomic Energy Agency (JAEA) in Tokai (Fig. 1). In 2003, the Neutron Scattering Laboratory was reorganized as the Neutron Science Laboratory to further promote the neutron science with use of the instruments in JRR-3. Under the General User Program supported by NSL, 14 university-group-owned spectrometers in the JRR-3 reactor are available for a wide scope of researches on material science, and proposals close to 300 are submitted each year, and the number of visiting users under this program reaches over 6000 person-day/year. In 2009, NSL and Neutron Science Laboratory (KENS), High Energy Accelerator Research Organization (KEK) built a chopper spectrometer, High Resolution Chopper Spectrometer, HRC, at the beam line BL12 of MLF/J-PARC

Fig. 1. The reactor of JRR-3. The eight neutron scattering instruments are attached to the horizontal beam tubes in the reactor experimental hall. Two thermal and three cold guides are extracted from the reactor core towards the guide hall located to the left.

(Materials and Life Science Experimental Facility, J-PARC). HRC covers a wide energy and Q-range ($10\mu eV < \hbar\omega < 2eV$ and $0.02Å^{-1} < Q < 50Å^{-1}$), and therefore becomes complementary to the existing inelastic spectrometers at JRR-3. HRC started to accept general users through the J-PARC proposal system in FY2011.

Triple axis spectrometers, HRC, and a high resolution powder diffractometer are utilized for a conventional solid state physics and a variety of research fields on hard-condensed matter, while in the field of soft-condensed matter science, researches are mostly carried out by using the small angle neutron scattering (SANS-U) and/or neutron spin echo (iNSE) instruments. The upgraded time-of-flight (TOF) inelastic scattering spectrometer, AGNES, is also available through the ISSP-NSL user program.

On March 11, 2011, a great earthquake with Magnitude 9.0 hit North East Coast of Japan. Fortunately, JRR-3 was under regular inspection and no serious accidents or damages were reported. However, the lifeline of Tokai Village area was lost for more than two weeks, and it took more than two months before damage inspection of JRR-3 could be started. As of May of 2013, JRR-3 has not restarted yet. General User Program of 2012 was cancelled and that of 2013 has been suspended so far. In order to compensate the loss of the activity of NSL, a number of proposals accepted in 2011 and 2012 were transferred to overseas thanks to kind offer from the major facilities, namely, ORNL, ILL, ANSTO, and HANARO.

Fig. 2. The U.S.-Japan spectrometer, CTAX, installed at the cold guide line CG4, High Flux Isotope Reactor (HFIR), in Oak Ridge National Laboratory. Members who contributed the relocation project of the U.S.-Japan spectrometer celebrates the completion of the project in October 2010.)

Research topics in FY2012 cover Hydrogen release from Li alanates originates in molecular lattice instability (6G: TOPAN T1-3:HERMES), Direct observation of antiferromagnetic ordering in s electrons confined in regular nanospace of sodalite (5G:PONTA), Structural analysis of high performance ion-gel comprising tetra-PEG networks (SANS-U), Neutron scattering studies of Ti-Cr-V bcc alloy with the residual hydrogen and deuterium (AGNES). In addition, there are a variety of activities on fundamental physics, neutron beam optics, developments of neutron scattering techniques.

The NSL also operates the U.S.-Japan Cooperative Program on neutron scattering, providing further research opportunities for material scientists who utilize the neutron scattering technique for their research interests. In 2010, relocation of the U.S.-Japan triple-axis spectrometer, CTAX, was completed, and it is now open to users (Fig. 2).
http://neutrons.ornl.gov/instruments/HFIR/CG4C/

The activity report on Neutron Scattering Research in FY2011 is given in NSL-ISSP Activity Report vol. 18 (2011), which can be downloaded from the following URL,
http://quasi.issp.u-tokyo.ac.jp/actrep/actrep-18-2011/index-rep_vol18.html

The list of publication is also given at,
(http://quasi.issp.u-tokyo.ac.jp/actrep/actrep-18-2011/index-pub_vol18.html).

International MegaGauss Science Laboratory

The objective of this laboratory (Fig.1) is to study the physical properties of solid-state materials (such as semiconductors, magnetic materials, metals, insulators, superconducting materials) under ultra-high magnetic field conditions. Such a high magnetic field is also used for controlling the new material phase and functions. Our pulse magnets, at moment, can generate up to 87 Tesla (T) in a non-destructive manner, and from 100 up to 730 T (the world strongest as an in-door record) by destructive methods.

They are open to scientists both from Japan and from overseas, especially from Asian countries, and many fruitful results are expected to come out not only from collaborative research but also from our in-house activities. One of

Fig. 1. Signboard at the entrance of the IMGSL.

Fig. 2. The building for the flywheel generator (left hand side) and a long-pulse magnet station (right hand side). The flywheel giant DC generator is 350 ton in weight and 5 m high (bottom). The generator, capable of a 51 MW output power with the 210 MJ energy storage, is planned to energize the long-pulse magnet generating 100 T without destruction.

our ultimate goals is to provide the scientific users as our joint research with magnets capable of a 100 T, milli-second pulses in a non-destructive mode, and to offer versatile precision physical measurements. The available measuring techniques now include magneto-optical measurements, cyclotron resonance, spin resonance, magnetization and transport measurements.

Our interests cover quantum phase transitions (QPT) induced by high magnetic fields. Field-induced QPT has been explored in various materials such as quantum spin systems, strongly correlated electron systems and other magnetic materials. Non-destructive strong pulse magnets are expected to provide us with reliable and precise solid state physics measurements. The number of collaborative groups for the research is over 50 in the year of 2012.

A 210 MJ flywheel generator (Fig.2) which is the world's largest DC power supply has been installed in the newly built

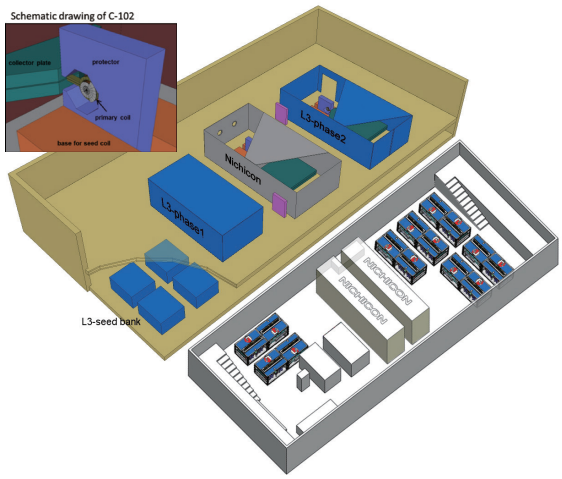

Fig. 3. (Build. C) The building for the electro-magnetic flux compression, generating over 700 T. 1000 T project started since 2010, and finally condenser banks of 9 MJ (5 MJ + 2 MJ +2 MJ) as a main system with the 2 MJ sub bank system for the seed field will be installed, and will be completed in the year of 2013.

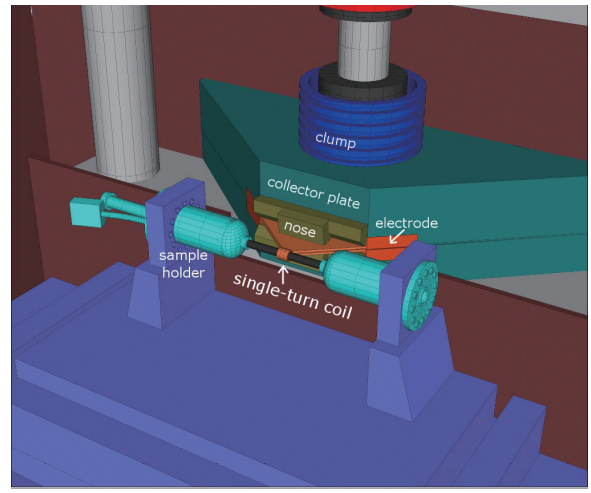

Fig. 4. Schematic picture of the H-type single-turn coil equipped with a 50 kV, 200 kJ fast operating pulse-power system, capable of generating 300 T within 3 mm bore coil.

DC flywheel generator station at our institute. The generator, once used for Toroidal magnet coil in JFT-2M (JAERI Fusion Torus-2M) Tokamak nuclear fusion testing device, is now renewed as a power supply for the pulse magnets. The construction of the magnet service station has also been accomplished. The magnet technologies are intensively devoted to the quasi-steady long pulse magnet (of order of 1-10 sec) energized by the giant DC power supply, and also used for the outer-magnet coil to realize a 100 T nondestructive magnet.

Developments of our destructive magnets are currently in progress. The ultra-high magnetic fields are obtained in a microsecond time scale. The electromagnetic flux compression (EMFC) system is equipped with a 5 MJ condenser bank and its seed coils with a 1.5 MJ condenser bank. The protector chamber and iron block protectors were refined against stronger explosion than before to be endurable against explosion by a full injection of 5 MJ. By devising copper lined primary coil, we could improve energy transfer efficiency from the primary coil to the liner kinetic energy compressing the magnetic flux. The seed field coils providing the initial magnetic flux are also newly designed and the maximum magnetic field was increased from 3.2 T to over 4.4 T at the position of the primary coil. These efforts led us to obtain the maximum magnetic field of 730 T by a 4 MJ injection of the EMFC recognized as a renewal of the world record as an indoor experiment. We have started a new project of the EMFC aiming at achieving 1000 T and its application to the materials science, financed by the ministry of education, culture, sports, science and technology in the fiscal year of 2010 and 2011 (Fig.3).

As an easy access to the megagauss science and technology, we have the single-turn coil (STC) system capable of generating the fields of up to 300 T by a fast-capacitor of 200 kJ. We have two STC systems, one is a horizontal type (H-type, Fig.4) and the other is a vertical type (V-type). Various kinds of laser spectroscopy experiments such as the cyclotron resonance and the Faraday rotation using the H-type STC are available. On the other hand, for very-low temperature experiments, a combination of the V-type STC and a liquid helium bath cryostat is very useful; the precise magnetization measurements at 2.5 K can be performed up to 120 T.

	Alias	Type	B_{max}	Pulse width Bore	Power source	Applications	Others
Building C Room 101-113	Electro- Magnetic Flux Compression	destructive	730 T	μs 10 mm	5 MJ, 40kV	Magneto-Optical Magnetization	5 K – Room temperature
	Horizontal Single-Turn Coil	destructive	300 T 200 T	μs 5 mm 10 mm	0.2 MJ, 50 kV	Magneto-Optical measurements Magnetization	5 K – 400 K
	Vertical Single-Turn Coil	destructive	300 T 200 T	μs 5 mm 10 mm	0.2 MJ, 40 kV	Magneto-Optical Magnetization	2 K – Room temperature
Building C Room 114-120	Mid-Pulse Magnet	Non-destructive	60 T 70 T	40 ms 18 mm 40 ms 10 mm	0.9 MJ, 10 kV	Magneto-Optical measurements Magnetization Magneto-Transport Hall resistance Polarization Magneto-Striction Magneto-Imaging Torque Magneto- Calorimetry Heat Capacity	Independent Experiment in 5 site Lowest temperature 0.1 K
Building C Room 121	PPMS	Steady State	14 T			Resistance Heat Capacity	Down to 0.3 K
	MPMS	Steady State	7 T			Magnetization	
Building K	Short-Pulse magnet	Non-destructive	87 T (2-stage pulse) 85 T	5 ms 10 mm 5 ms 18 mm	0.5 MJ, 20 kV	Magnetization Magneto-Transport	2K – Room temperature
	Long-Pulse magnet	Non-destructive	30 T	0.5 s 30 mm	210 MJ, 2.7 kV	Resistance Magneto-Calorimetry	2K – Room temperature

Table 1. Available Pulse Magnets, Specifications

Center of Computational Materials Science

K-computer at Kobe won the title of the world's fastest computer at TOP500 ranking announced at International Supercomputing Conference (ISC) 11. Though it is in the 3rd place in the list as of today, it is still providing the Japanese scientific community with an incomparable amount of computational resources. With the advancement of hardware and software technologies, large-scale numerical calculations have been making important contributions to materials science and will have even greater impact on the field in the near future. Center of Computational Materials Science (CCMS) was founded as a specialized research center for promoting computer-aided materials science with massively parallel computation using K-computer. This center also functions as the headquarters of Computational Materials Science Initiative (CMSI), which is an inter-institutional organization for computational science of a broad range of disciplines, including molecular science, quantum chemistry, biological materials, and solid state physics. ISSP made contracts with 9 universities and 2 national institutes for supporting the activities of CMSI in which nearly 100 research groups are involved. The main purpose of CMSI is to establish a new community of computational science in which researches from different backgrounds work together on grand challenge problems, thereby developing computational infrastructures (new algorithms, coding styles, standard software packages, etc) and inspire young scientists.

A branch office of CCMS was also established in the RIKEN AICS building on the Port Island Kobe, where K-computer is located, for supporting CMSI researchers getting together at Kobe to fine-tune various applications software for K-computer. It also helps developing better contact with staff members of RIKEN, the operating institute of K-computer. Another mission of the Kobe branch of CCMS is exchanging ideas and techniques with researchers from other fields of computer science. (There are 5 major

Fig. 1. K-Computer

Fig. 2. Summer School in Zao

fields in the HPCI strategic program of MEXT, "biology", "materials and energy" (our field), "seismology, oceanography and meteorology", "industrial applications", and "high-energy physics and cosmology".)

The following is the selected list of meetings organized by CMSI and CCMS in SY2012:

- "K-Computer Users' Forum" (May 10/2012, Kobe)
- "Joint-Meeting between Field 2 and 5" (May 30/2012 Kashiwa)
- "Material Simulation in Petaflops Era (MASP) 2012" (June 25-July 13/2012, Kashiwa)
- "Workshop: Programming Techniques for K-Computer" (July 17-19/2012, Kakegawa)
- "Summer School: New Materials and New Quantum States" (Aug. 20/2012, Zao)
- "RSC-CMSI Joint Symposium: Multi-scale Structures Research" (Sep. 15/2012, Hyogo)
- "CMSI Symposium" (Dec. 03-05/2012, Okazaki)
- "Interdisciplinary Workshop on Numerical Methods for Many-Body Correlations" (Feb. 05-06/2013, Hongo)
- "CMSI Kobe Hands-On: FMO Tutorial" (Feb. 07/2013, Kobe)
- "Workshop on Synchrotron Radiation and Computational Physics" (Feb. 14/2013, Hongo)
- "Workshop: Programming Techniques for K-Computer" (Feb. 14-16/2013, Kanazawa)
- "Symposium: Visualization of Materials Science" (Mar. 05/2013, Akihabara)
- "CMSI Kobe Hands-On: ALPS Tutorial" (Mar. 06/2013, Kobe)
- "CMSI Kobe Hands-On: xTAPP Tutorial" (April 23/2013, Kobe)

Synchrotron Radiation Laboratory

The Synchrotron Radiation Laboratory (SRL) was established in 1975 as a research division dedicated to solid state physics using synchrotron radiation (SR). In 1989, SRL started to hold the Tsukuba branch, a branch laboratory in the Photon Factory (PF), High Energy Accelerator Research Organization (KEK). SRL maintains a Revolver undulator, two beamlines and three experimental stations; BL-18A for angle-resolved photoemission spectroscopy with SCIENTA electron analyzer, while undulator beamline BL-19A and BL-19B, for spin- and angle-resolved photoelectron spectroscopy (SARPES) and soft X-ray emission spectroscopy experiments, respectively. Recently, a high-yield spin detector, using very low energy electron diffraction, was developed at BL-19A. SAPRES measurements have now been performed with high-resolution and the experiments at the beamline have become important for exciting topics of surface/solid state physics such as topological insulators and ferromagnetic nanofilms.

The SRL staffs have joined the Materials Research Division of the Synchrotron Radiation Research Organization (SRRO) of the University of Tokyo and they have played essential role in constructing a new high brilliant soft X-ray beamline, BL07LSU, in SPring-8. The light source is the polarization-controlled 25-m long soft X-ray undulator. The monochromator is equipped with varied-line-spacing plain grating, which covers the photon energy range from 250 eV to 2 keV. At the end of the beamline, four experimental stations have been developed for frontier spectroscopy researches: the three-dimensional (3D) nano-ESCA station, the soft X-ray emission spectroscopy (XES) station, the time-resolved soft X-ray spectroscopy (TR-SX) station, and the free-port station for any experimental apparatus.

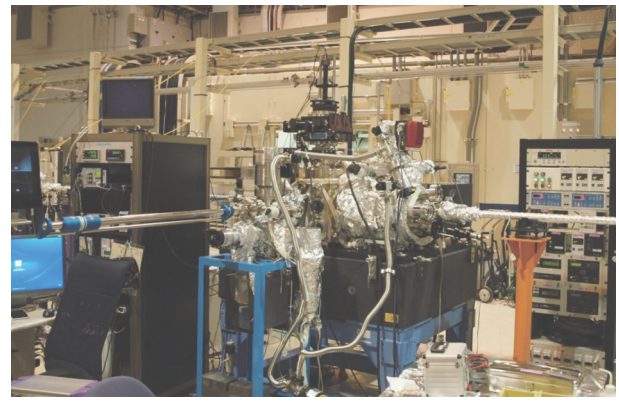

Fig. 1. 3D nano ESCA at SPring-8 BL07LSU

Fig. 2. XES station at SPring-8 BL07LSU

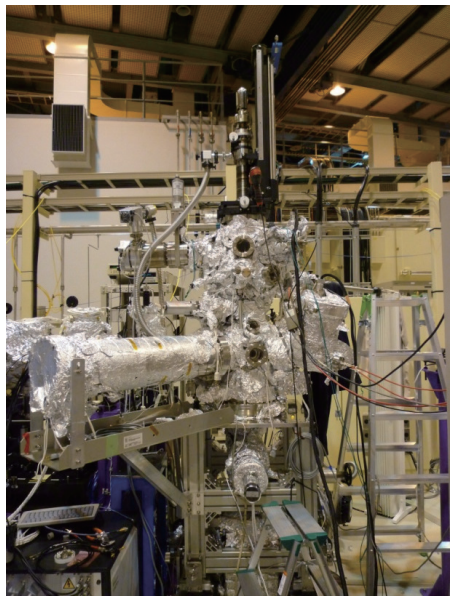

Fig. 3. TR-SX station at SPring-8 BL07LSU

The beamline construction was completed in 2009 and SRL established the Harima branch laboratory in SPring-8. The four end-stations have now been opened fully to outside users. In 2012, 110 researchers made their experiments during the SPring-8 operation time of 4000 hours.

Members of SRL have devoted themselves in serving users with technical supports and they have also carried out their own research works on advanced solid state spectroscopy. At SPring-8 BL07LSU, for example, the staffs have achieved the high performance at their stations: the 3D nano-ESCA reaches the spatial resolution of 70 nm, the XES station obtains spectra with energy resolving power E/ΔE larger than 10,000, and the TR-SX makes the laser –pump and SR-probe method with the time-resolution of 50 ps which corresponds to the SR pulse-width.

Laser and Synchrotron Research Center

Laser and Synchrotron Research (LASOR) Center started from October, 2012. LASOR center consists of extreme laser groups and Synchrotron Radiation Laboratory. LASOR center develops new lasers with extreme performance of ultra-precise, high intensity and ultra-short pulse lasers, and the cutting edge synchrotron radiation beamline in soft X-ray region. LASOR center is responsible for the advanced spectroscopy, such as ultra-high resolution photoemission,

Fig. 1. Open ceremony of LASOR center

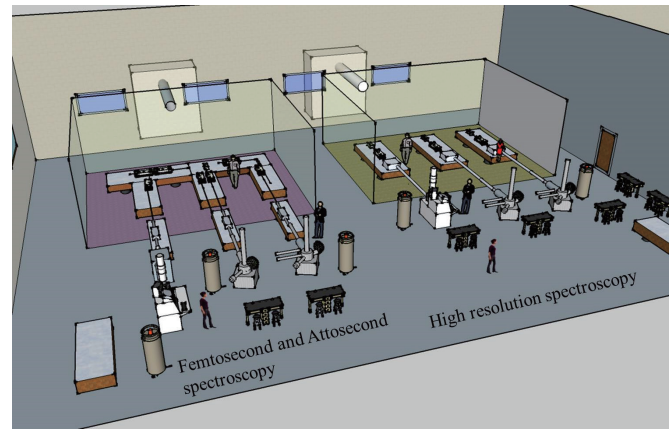

Fig. 2. Image of laser activities in Building E

time-resolved, spin-resolved spectroscopy, diffraction, light scattering, imaging, microscopy and fluorescence spectroscopy, by new coherent light sources based on laser and synchrotron radiation technology over a wide spectrum range from terahertz to soft X-ray. In LASOR center, a variety of materials sciences, such as semiconductors, strongly-correlated materials, molecular materials, surface and interfaces, and bio-materials, are studied using advanced light sources and advanced spectroscopy. Another aim of LASOR center is to promote the collaboration between the advanced photon sciences and materials sciences. Most of the research activities on the development of new lasers with an extreme performance and the application to material science are studied in specially designed Buildings D and E with large clean rooms and the isolated floor in Kashiwa Campus. On the other hand, the experiments utilizing the synchrotron radiation are performed at beamline BL07LSU in SPring-8 (Hyogo) by Synchrotron Radiation Laboratory in LASOR center.

Unconventional Magnetic and Thermodynamic Properties of S = 1/2 Spin Ladder with Ferromagnetic Legs

H. Yamaguchi and T. Sakakibara

Spin-ladder systems have been investigated both theoretically and experimentally in relation in particular to field-induced quantum phase transitions and high-T_c superconductivity. Among these systems, antiferromagnetic (AFM) two-leg spin ladders, which have AFM rung and leg interactions, have been most extensively studied and have turned out to show attractive behaviors originating from their strong quantum fluctuations. By contrast, a spin ladder with ferromagnetic (FM) leg interactions, which can be viewed as antiferromagnetically coupled FM chains, has not been realized experimentally. Its ground state and the magnetic behavior have been discussed extensively from a theoretical point of view as an example of complicated quantum spin systems. The experimental verification of these properties is thus quite significant for studies on complicated quantum behavior unsuspected in conventional spin systems.

Here, we report the first model compound of an S = 1/2 two-leg spin ladder with FM leg interaction [1]. We have succeeded in synthesizing a new verdazyl radical 3-Cl-4-F-V [3-(3-chloro-4-fluorophenyl)-1,5-diphenylverdazyl] and solved its crystal structure. The *ab initio* molecular orbital (MO) calculation indicated the formation of an S = 1/2 two-leg spin ladder with FM leg and AFM rung interactions. The experimental results of magnetic susceptibility, magnetization curve, and specific heat were successfully explained as the expected spin-ladder model by using the quantum Monte Carlo method.

Figures 1(a) and 1(b) show the low-temperature region of the magnetic susceptibility and magnetic specific heat in various magnetic fields, respectively. At higher magnetic fields, we observed extrema of the magnetic susceptibility, which appear almost symmetrically with respect to the curve at 3.0 T. Regarding the magnetic specific heat, the anomaly observed at zero field splits into two peaks above 1.5 T, as shown in Fig. 1(b). Figure 2 shows the temperature-field phase diagram obtained from those specific temperatures. The transition point shifts toward the high-temperature region with an increasing magnetic field up to 3.0 T. This type of phase boundary shape is often associated with the field-induced phase transition in a gapped spin system. Since

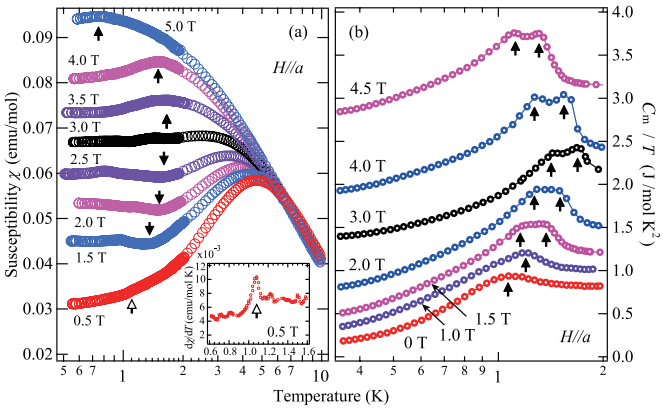

Fig. 1. Temperature dependence of (a) the magnetic susceptibility and (b) C_m/T of 3-Cl-4-F-V in various magnetic fields for $H//a$. The arrows indicate the phase transition temperatures. For clarity, C_m/T for 1.0, 1.5, 2.0, 3.0, 4.0, and 4.5 T have been shifted up by 0.2, 0.4, 0.7, 1.3, 1.7, and 2.5 J•mol^{-1}•K^{-2}, respectively. The inset shows the temperature derivative of the magnetic susceptibility at 0.5 T.

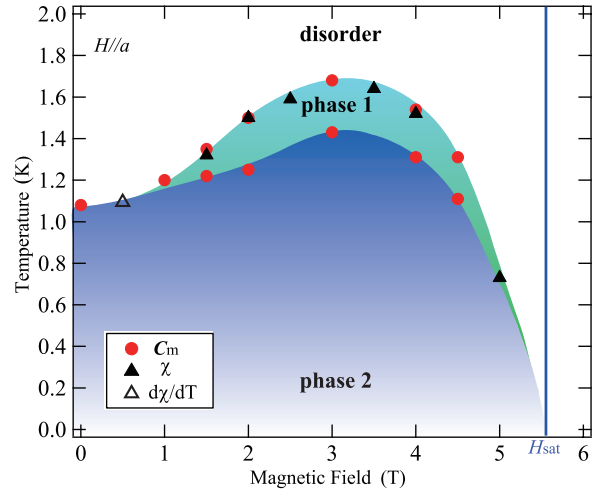

Fig. 2. Magnetic field versus temperature phase diagram of 3-Cl-4-F-V for $H//a$ The closed circles, closed, triangles, and open triangle indicate the transition temperatures determined from the magnetic specific heat, the magnetic susceptibility, and its temperature derivative, respectively. The solid vertical line indicates the saturation field.

the expected small energy gap of 1.06 K is considered to disappear owing to the weak interladder interactions, the present system must be in the vicinity of the quantum critical point between the gapped rung-singlet and the gapless ordered phases. Considering the magnetic specific heat, we should take into account the possibility of successive phase transitions, which is often induced by large magnetic anisotropy and/or noncollinear magnetic structure. Since organic radical systems have negligibly weak magnetic anisotropy, we can suggest the possibility of noncollinear magnetic structure induced by frustration. The MO calculation indicated that there are three kinds of possible small interladder interactions. These three interactions can form frustrated lattices, and then a noncollinear magnetic structure will appear. This unexpected field-induced successive phase transition possibly originates from the interplay of low dimensionality and frustration. The present results will stimulate studies on spin ladder with FM interactions and unconventional behavior of the complicated quantum spin systems.

Reference

[1] H. Yamaguchi, K. Iwase, T. Ono, T. Shimokawa, H. Nakano, Y. Shimura, N. Kase, S. Kittaka, T. Sakakibara, T. Kawakami, and Y. Hosokoshi, Phys. Rev. Lett. **110**, 157205 (2013).

Authors
H. Yamaguchi[a], K. Iwase[a], T. Ono[a], T. Shimokawa[b], H. Nakano[c], Y. Shimura, N. Kase, S. Kittaka, T. Sakakibara, T. Kawakami[c], and Y. Hosokoshi[a]
[a]Osaka Prefecture University
[b]Kobe University
[c]University of Hyogo
[d]Osaka University

Axion Electrodynamics and Condensed Matter

H. Ooguri and M. Oshikawa

Condensed matter physics and high-energy physics deal with phenomena at very different scales. Nevertheless, surprisingly often we encounter similar mathematical structures in these two different subfields of physics. Indeed, those encounters have been very fruitful for new devel-

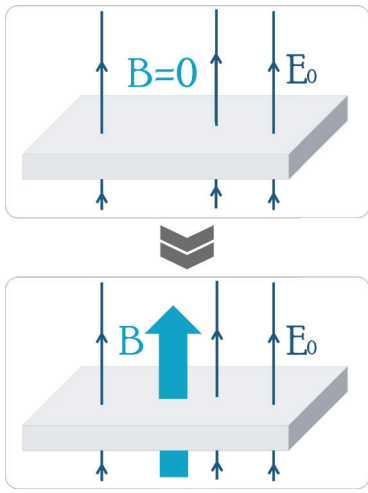

Fig. 1. The phase transition of the "axion" field takes place under an applied electric field E_0 above the critical value. It results in a spontaneous generation of magnetic field, even though no magnetic field is applied externally. (Figure drawn by Euan McKay and Azusa Minamizaki, reprinted from Todai Research Editor's Choice: http://www.u-tokyo.ac.jp/en/todai-research/editors-choice/theory-of-undiscovered-elementary-particle-applied-to-topological-insulator/)

opments in physics: notable examples include Nambu' s development of spontaneous symmetry breaking in field theory with a hint from superconductivity, and Wilson's renormalization group unifying critical phenomena and field theory. Very recently, application of AdS/CFT correspondence to condensed matter is actively pursued. The foundation of IPMU (Institute for Physics and Mathematics of the Universe, now Kavli IPMU) in 2007 and opening of its building next to ISSP in 2010 provides a great opportunity for ISSP. In 2010, IPMU and ISSP co-hosted a workshop "Condensed Matter Physics Meets High-Energy Physics" to stimulate exchanges between the two fields.

Here we report on a recent joint research [1] between the two institutes. "Axion" is a hypothetical elementary particle, which has not yet been detected experimentally, but could be a key to solve mysteries in high-energy physics and cosmology. Recently, instability of axion field in the presence of strong electric field has been pointed out in high-energy physics. While the original axion as an elementary particle would not directly appear in condensed matter, it was pointed out [2] that doping of magnetic ions to a topological insulator results in fluctuating magnetic moments, which could be described by a similar field theory as the one of axions. We investigated the instability of the "axion" field in the condensed matter realization. It also led to a understanding of the physical mechanism of the instability, and to the clarification of the final state reached as a result of the instability. Above a critical electric field, magnetic field is spontaneously generated, and the excess electric field is screened by the effective surface charge induced by the deformation of the "axion" field and the magnetic field.

References
[1] H. Ooguri and M. Oshikawa, Phys. Rev. Lett. **108**, 161803 (2012).
[2] R. Li, J. Wang, X.-L. Qi, and S.-C. Zhang, Nature Phys. **6**, 284 (2010).

Authors
H. Ooguri[a] and M. Oshikawa
[a]Kavli IPMU and California Institute of Technology

Band-Gapped Graphene Nanoribbons Made by Molecular Beam Epitaxy

S. Tanaka and F. Komori

Graphene nanoribbons (GNRs) are attracting much attention in solid state physics and nanoelectronic applications, where the band-gap opening or modification of the electronic structure at K-points is a central interest. The electronic structure at K-points in GNRs has been theoretically shown to depend on the type of edge geometry: armchair or zigzag [1]. Semiconducting characteristics are expected in the case of armchair edges owing to the band-gap opening at K-points. As the width of GNRs is reduced, the gap is increased by both electron confinement and edge effects. However, realization of GNRs with atomically well-defined edges and providing experimental evidences of the gap opening at K-points remain challenging. Here we demonstrate a new approach for producing a dense array of aligned GNRs on unique SiC surfaces [2] as templates via molecular beam epitaxy (MBE), and show band-gap openings at K-points visualized by angle-resolved photoemission spectroscopy (ARPES) [3].

In the present study, we used an off-axis SiC substrate (Si-face, 4º off toward [1-100]), and first prepared a self-ordered periodic structure consisting of pairs of a (0001) basal plane terrace and a (1-10*n*) nanofacet (*n* = 35~37) with a characteristic periodicity of ~ 20 nm by H_2 gas etching [2]. A typical atomic-force-microscopy (AFM) image of the substrate and a model are shown in Fig. 1. After cleaning the surface of the substrate under Si flux at 1050ºC, a carbon mono-atomic layer with $(6\sqrt{3}\times6\sqrt{3})$R30º registry was grown exclusively on the SiC terrace by MBE. Finally, the samples were exposed to H_2 gas at 600ºC for 1 h to transform the carbon layer into quasi-free-standing graphene by hydrogen intercalation. The GNRs thus made have armchair edges parallel to the step edge of the substrate. Quality of the graphene was evaluated by AFM, scanning tunneling microscopy, reflection high-energy electron diffraction, low-energy electron diffraction, and Raman spectroscopy.

Figure 2(a) shows the ARPES result along the Γ-K-M lines of the graphene surface Brillouin zone. The measured Γ-K-M direction in k-space corresponds to the [1-100] direction in real space, which is perpendicular to the edges of the GNRs. A conduction band is invisible, and the valence band is folded at the K-point area, as shown in Fig. 2(b). No states are detected at the K-point between the Fermi energy (E_F) and top of the valence band, which is 0.14 eV below E_F.

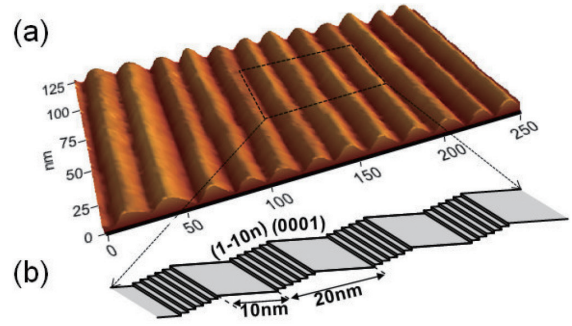

Fig. 1. (a) An AFM 3-dimensional view of the vicinal SiC(0001) surface after hydrogen etching, showing a periodic array of terrace and facet structure. (b) A schematic drawing of the SiC surface in (a). This was derived from high-resolution transmission electron microscopy images. Each pair of array consists of the (0001) terrace and (1-10*n*) facet, and is ordered with the periodic distance of ~ 20 nm. Here, *n* = 35 ~37. The width of each (0001) terrace is ~ 10 nm.

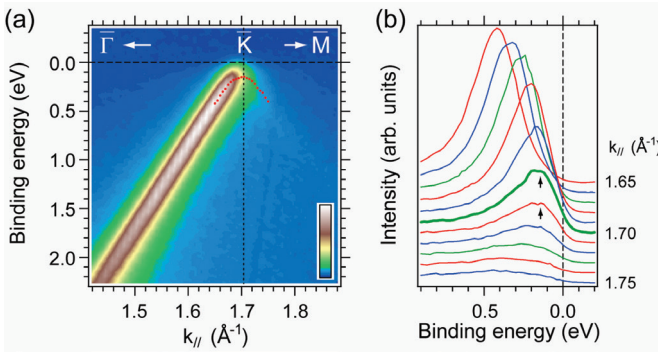

Fig. 2. Intensity map (a) and energy distribution curves (EDCs) (b) of the ARPES spectra around the K-point for the GNRs on the vicinal SiC(0001) substrate. The spectra are taken along the Γ-K-M line. The EDCs show the folding of the valence band at the K-point below E_F. The red dots in (a) indicate the positions of the EDC peaks and represent band dispersion around the K-point. The intensity map indicates a linear dispersion, which is consistent with the valence band of single-layer graphene.

The band-gap value can be more than 0.28 eV if we assume a slight p-type doping in the sample as in the case of the hydrogen-intercalated graphene on SiC(0001). This value is consistent with the theoretical estimation for the GNR with the width of 10 nm.

References
[1] K. Nakada *et. al.*, Phys. Rev. B **54**, 17954 (1996).
[2] H. Nakagawa *et. al.*, Phys. Rev. Lett. **91**, 226107 (2003).
[3] T. Kajiwara *et. al.*, B **87**, 121407(R) (2013).

Authors
T. Kajiwara[a], Y. Nakamori[a], A. Visikovskiy[a], T. Iimori, F. Komori, K. Nakatsuji[b], K. Mase[c], and S. Tanaka[a]
[a]Kyushu University
[b]Tokyo Institute of Technology
[c]High Energy Accelerator Research Organization

Spin Filtering in Oxide Tunnel Junctions

I. Ohkubo, T. Harada, and M. Lippmaa

The operation of conventional functional tunnel devices, such as tunnel magnetoresistance junctions or Josephson junctions, is derived from the physical properties of the electrode materials, such as soft ferromagnets or superconductors. The tunnel barrier is usually a passive element in a junction, simply providing a suitable separation between the functional electrodes. The appearance of a ferromagnetic insulator state in mixed-valent manganites opens a possibility to construct a different type of junction, where the electrodes are passive and the functional element is the tunnel barrier itself. The junctions developed in this project contain tunnel barriers made of 10 to 12 unit cells of $Pr_{0.8}Ca_{0.2}Mn_{1-y}Co_yO_3$ [1]. The ferromagnetic insulating state can be achieved by a suitable Pr/Ca ratio, while the saturation magnetization can be adjusted by Co doping. The electrodes of the junctions were made of a normal metal $LaNiO_3$ and a ferromagnetic metal $La_{0.6}Sr_{0.4}MnO_3$, as illustrated in Fig. 1. Electrons tunneling from the $LaNiO_3$ electrode to the $La_{0.6}Sr_{0.4}MnO_3$ side see different barrier heights, depending on spin state, due to an exchange splitting in the magnetic barrier layer. The spin injection rate into the ferromagnetic $La_{0.6}Sr_{0.4}MnO_3$ electrode is thus different for spin-up and spin-down electrons.

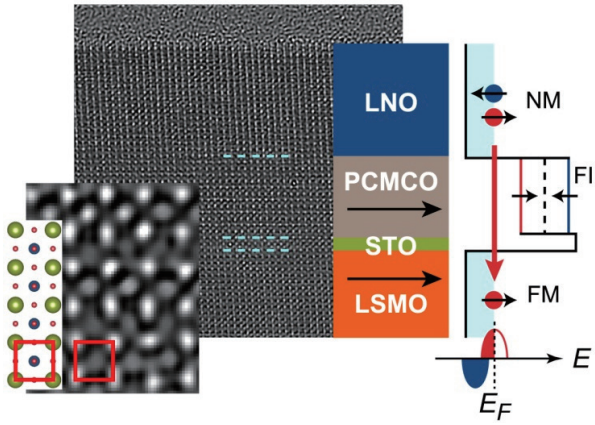

Fig. 1. Cross-sectional electron microscope image and a schematic diagram of a spin-filter tunnel junction consisting of normal metal (NM) $LaNiO_3$ (LNO) injection electrode, a $Pr_{0.8}Ca_{0.2}Mn_{1-y}Co_yO_3$ (PCMCO) tunnel barrier, a $SrTiO_3$ (STO) spacer, and a ferromagnetic (FM) spin detector $La_{0.6}Sr_{0.4}MnO_3$ (LSMO).

The $La_{0.6}Sr_{0.4}MnO_3$ layer in the junction works not only as a metallic electrode but also as a built-in ferromagnetic spin detector. Due to strong spin polarization in $La_{0.6}Sr_{0.4}MnO_3$, a spin-filtered tunneling current can only flow through the device when the magnetization directions in the ferromagnetic barrier and electrode layers are parallel. The efficiency of the tunnel barrier spin filter can therefore be determined easily by measuring the junction resistance as a function of an applied magnetic field (Fig. 2). Such a plot shows high resistance when the applied field is has just changed sign and the magnetically soft $La_{0.6}Sr_{0.4}MnO_3$ electrode layer magnetization has flipped antiparallel to the tunnel barrier layer. Above the coercive field of the barrier layer, at an applied field of about 200 mT, the whole device magnetizes in the same direction and the total resistance drops sharply. The magnetoresistance ratio of over 100% is among the largest seen for any spin-filter junction.

Spin-filter junctions have several interesting uses, the most important being an efficient spin injector for semiconducting spintronic devices. Since the material in contact with a semiconductor is insulating, a spin-filter tunnel junction injector does not suffer from an impedance mismatch that occurs when a ferromagnetic metallic electrode is used as a spin-polarized current source in a semiconductor device. Analysis of spin filter efficiencies and inelastic electron tunneling spectroscopy showed that the choice of the normal metal electrode material is important in achieving efficient spin injection [2]. The use of a perovskite-type $LaNiO_3$ electrode that was lattice matched (Fig. 1) with the insulator layer greatly increased the magnetoresistance ratio of the junctions, indicating improved spin filtering contrast. An approximate matching of the Fermi surface shapes

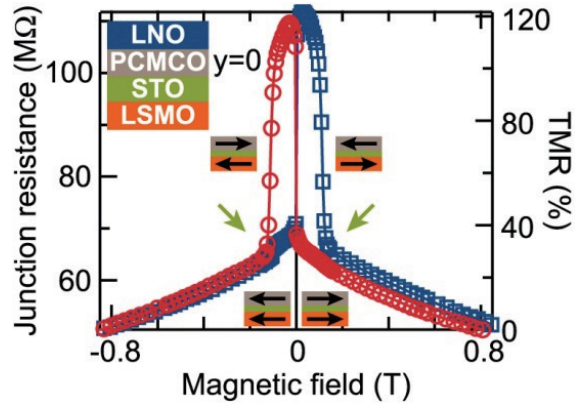

Fig. 2. Tunnel magnetoresistance response of a spin-filter tunnel junction at 4 K, showing a resistance switching ratio of over 100%.

of the electrode materials appeared to reduce scattering of tunneling electrons, further improving the spin filter efficiency.

References

[1] T. Harada, I. Ohkubo, M. Lippmaa, Y. Sakurai, Y. Matsumoto, S. Muto, H. Koinuma, and M. Oshima, Adv. Funct. Mater. **22**, 4471 (2012).

[2] T. Harada, I. Ohkubo, M. Lippmaa, Y. Sakurai, Y. Matsumoto, S. Muto, H. Koinuma, and M. Oshima, Phys. Rev. Lett. **109**, 076602 (2012).

Authors

T. Harada, I. Ohkubo[a,b], M. Lippmaa, Y. Sakurai[b], Y. Matsumoto[c], S. Muto[d], H. Koinuma[e,f] and M. Oshima[b]

[a]National Institute for Materials Science
[b]Department of Applied Chemistry, University of Tokyo
[c]Tokyo Institute of Technology
[d]Nagoya University
[e]Graduate School of Frontier Sciences, University of Tokyo
[f]Pusan National University

Anisotropy of Upper Critical Field in a One-Dimensional Organic System, $(TMTTF)_2PF_6$ under High Pressure

M. Kano and M. Itoi

The Bechgaard salt $(TMTSF)_2PF_6$ (TMTSF = tetramethyltetraselenafulvalene) was the first organic superconductor discovered in 1980 with a superconducting temperature of Tc = 0.9 K (critical pressure, Pc =1.2 GPa) [1]. Since this discovery, materials based on TMTSF and its derivatives, such as TMTTF (tetramethyltetrathiofulvalene), the so-called $(TMTCF)_2X$ (X = monovalent anion) series, have been investigated extensively to search for other superconducting behaviors. They also attracted attention owing to their rich properties such as spin-Peierls (SP), charge-ordering (CO), spin density wave (SDW), and possible unconventional superconductivity (SC) that appear by changing the counter anion or by applying external pressure [2]. Many compounds with TMTSF molecules exhibit an SC state at low pressures of approximately 1 GPa, whereas most compounds with TMTTF exhibit an SC transition at ultra high pressures, for example, P_c= 5 GPa in $(TMTTF)_2PF_6$ [3,4,5]. Taking advantage of the low pressure induced and ambient pressure superconductivity, the characteristic for SC phase has been well studied with TMTSF salts, but rarely with TMTTF salts owing to the technical difficulty in applying hydrostatic pressure to the fragile organic compounds at low temperatures in magnetic fields. Recently, we have succeeded in resistivity measurement by using a turnbuckle-type Diamond anvil cell (DAC) on $(TMTTF)_2PF_6$ under multi-extreme conditions which was previously difficult to achieve [6]. We report on the characteristic superconductivity on $(TMTTF)_2PF_6$.

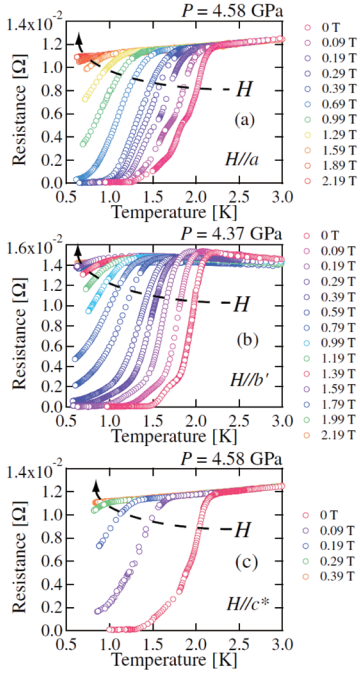

Fig. 1. The temperature-dependent resistivity of $(TMTTF)_2PF_6$ was measured up to 7 GPa using a turnbuckle-type diamond anvil cell (DAC) and at magnetic fields of up to 5 T. The applied magnetic fields were (a) parallel to the a-axis at P =4.58 GPa, (b) b'-axis at P = 4.37 GPa and (c) c*-axis at P = 4.58 GPa.

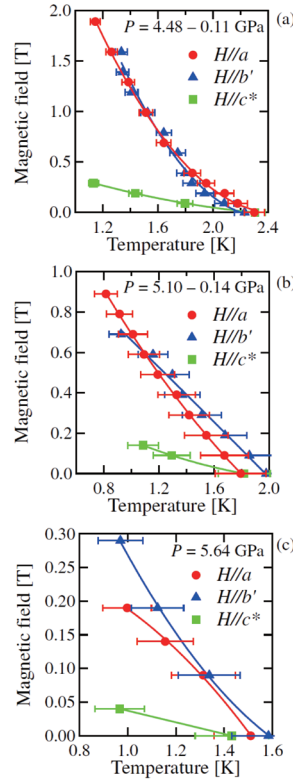

Fig. 2. H_{c2} curves with applied fields $H \parallel a$, $H \parallel b$' and $H \parallel c$* for P = (a) 4.48, (b) 5.10 and (c) 5.64 GPa obtained by using the onset criterion.

Data of resistivity vs temperature at P = 4.37-4.58 GPa with the field along three different axes are shown in Fig. 1, and the temperature dependence of H_{c2} along the three axes on $(TMTTF)_2PF_6$ is described in Fig. 2.

The H_{c2} has a positive curvature without saturation, which may be attributed to an FFLO state, for a magnetic field along the a (intra-chain direction) – and b'(inter-chain direction)- axes at $T \geq 0.5$ K for P = 4.48 GPa. We also have shown that the upturn feature is suppressed with increasing pressure and the orbital pair breaking mechanism becomes dominant. In further studies of the pair breaking mechanism,

measurement should be conducted at lower temperatures and with more refined pressure control. Our data above $T = 0.5$ K shows that H_{c2} slightly exceeds the Pauli paramagnetic limit at P =4.48 GPa for $H \parallel a$. H_{c2} curves for $H \parallel a$ and $H \parallel b$' lie on top of each other indicating that it has a two-dimensional-like feature, being isotropic within the ab' -plane. GL coherence lengths were obtained, which are highly anisotropic, for example, $\xi_a : \xi_{b'} : \xi_c = 5 : 5 : 1$ at $P = 5.64$ GPa. The interlayer coherence length ξ_c is much larger than the thickness of the conducting sheet for all pressures, which is $c/2 \sim 6.5$ Å , where c is a lattice parameter of $(TMTTF)_2PF_6$. These results revealed that $(TMTTF)_2PF_6$ is an anisotropic three-dimensional superconductor.

References

[1] D. Jérome, A. Mazaud, M. Ribault, and K. Bechgaard, J. Phys. Lett. **41**, 95 (1980).
[2] D. Jérome, Science **252**, 1509 (1991).
[3] T. Adachi, E. Ojima, K. Kato, H. Kobayashi, T. Miyazaki, M. Tokumoto, and A. Kobayashi, J. Am. Chem. Soc. **122**, 3238 (2000).
[4] D. Jaccard, H. Wilhelm, D. JeÅLrome, J. Moser, C. Carcel, and J. M. Fabre, J. Phys.: Condens. Matter **13**, L89 (2001).
[5] C. Araki, M. Itoi, M. Hedo, Y. Uwatoko, and H. Mori, J. Phys. Soc. Jpn. **76**, Suppl. A 198 (2007).
[6] M. Kano, H. Mori, K. Matsubayashi, M. Itoi, M. Hedo, T. P. Murphy, S. W. Tozer, Y. Uwatoko, and T. Nakamura, J. phys. Soc. Jpn. **81**, 024716 (2012).

Authors

M. Kano[a], H. Mori, K. Matsubayashi, M. Itoi[b], M. Hedo[c], T. P. Murphy[d], S. W. Tozer[d], Y. Uwatoko, and T. Nakamura[e]
[a]Tohoku University
[b]Nihon University
[c]University of the Ryukyu
[d]National High Magnetic Field Laboratory
[e]Institute for Molecular Science

Topological Hall Effect in Spin Ice Conduction Systems - Application to Exotic Hall Response in $Pr_2Ir_2O_7$ -

M. Udagawa

Topological Hall effect (THE) is a hallmark of modern condensed matter physics. We have addressed the THE in conduction electron systems interacting with spin ice, which is one of the prototypical magnetic states arising from geometrical frustration. This setting is relevant to $Pr_2Ir_2O_7$, where conduction electrons due to Ir 5d bands interact with Pr magnetic moments forming spin ice. In this compound, Hall conductivity shows highly non-monotonous and anisotropic behavior [1], while the conventional mechanisms of Hall conductivity lead to monotonously increasing Hall conductivity with magnetic field.

To address this peculiar Hall response, we started with the construction of general theory of THE in spatially inhomogeneous systems. As the simplest case, we considered Ising Kondo lattice model on a kagome lattice with [111]-type easy-axes anisotropy. Through the numerical diagonalization of this model, we found a characteristic crossover with respect to spin-electron coupling, J (Fig 1. (a)). For small J, the Hall conductivity is scaled as $\propto J^3$, where real-space spin scalar chirality spanned by three localized spins acts as an independent skew scatterer. On the other hand, for large J, the Hall conductivity converges to a finite value, where the electron spins are forced to align parallel to the localized moments.

Motivated by the clear identification of J^3 scaling in

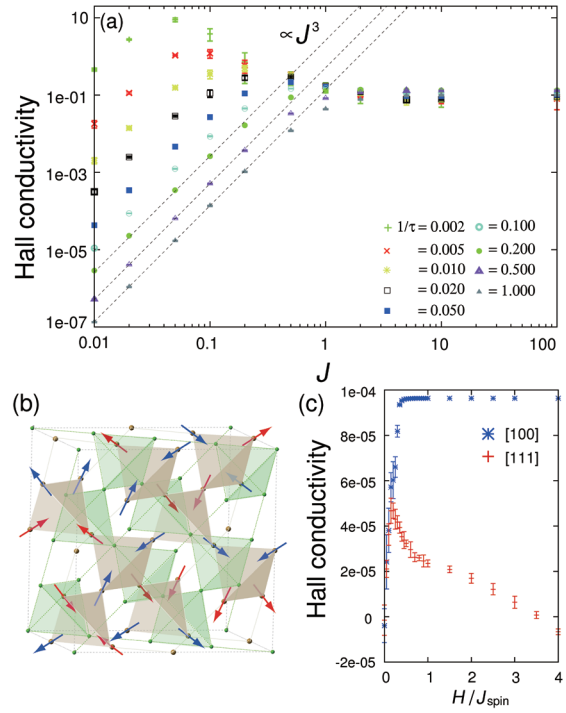

Fig. 1. (a) J and damping rate dependence of Hall conductivity of the Ising Kondo lattice model on a kagome lattice. Clear J^3 scaling can be observed in a weak-coupling region. (b) Schematic picture of double pyrochlore lattice. On one sublattice (brown), localized moments reside, while on the other (green), conduction electrons are defined. (c) Magnetic field dependence of Hall conductivity in the Ising Kondo lattice model on a double pyrochlore lattice. Steep kink is observed for H||[111], signaling the onset of kagome ice correlation.

weak coupling region, we applied the third-order perturbation theory [2] to the Hall conductivity of $Pr_2Ir_2O_7$, in which the coupling between conduction electrons and Pr moments arises from superexchange process and is small. To describe this compound, we adopt the Ising-type Kondo lattice model on a double pyrochlore lattice, where conduction electrons defined on one pyrochlore sublattice interact with localized Ising moments residing on the other pyrochlore sublattice (Fig 1. (b)). We calculate Hall conductivity by combining the third-order perturbation theory and Kubo formula.

As a result, we could successfully reproduce the non-monotonic behavior of Hall conductivity (Fig 1. (c)). In particular, for [111] magnetic field, the Hall conductivity shows steep peak at a relatively low field, then decreases, leading to sign reversal. These results well capture the main features of experimental data. One of the main implications of our analysis is that the peak for H||[111] can be associated with the crossover from zero-field spin ice state to kagome-ice-like state[3]. So far, this peak has been associated with the spin ice (2-in 2-out) to fully saturated state (3-in 1-out and 1-in 2-out)[1,4]. We thank R. Moessner for fruitful discussions.

References

[1] Y. Machida *et al*., Phys. Rev. Lett. **98**, 057203 (2007).
[2] G. Tatara and H. Kawamura, J. Phys. Soc. Jpn. **73**, 2624 (2004).
[3] M. Udagawa and R. Moessner, submitted to Phys. Rev. Lett.
[4] T. Tomizawa and H. Kontani, Phys. Rev. B **82**, 104412 (2010).

Author

M. Udagawa
University of Tokyo

Direct Observation of Antiferromagnetic Order by Neutron Diffraction of s-Electrons Confined in Regular Nanospace of Sodalite

T. Nakano and M. Matsuura

Various kinds of magnetically ordered state, such as ferromagnetism, antiferromagnetism, and ferrimagnetism, have been found in alkali metal nanoclusters arrayed in regular nanospace of aluminosilicate zeolite crystals. The magnetic properties depend on the zeolite framework structures, the species of alkali element and the electron density of the clusters. They are quite a new class of magnetic materials because the magnetic orderings are realized by the mutual interaction between s-electrons confined in the nanospace and they contain no magnetic elements such as transition metal or rare earth metal. In this article, we report the first direct observation of long-range magnetic ordering of s-electrons by neutron diffraction (ND) [1].

Sodalite is a kind of aluminosilicate zeolites. As shown in Fig. 1 (a), truncated-octahedron-shaped β-cages are arrayed in a body-centered cubic (bcc) structure. The inside diameter of the β-cage is approximately 0.7 nm. The framework $Al_3Si_3O_{12}$ is negatively charged and three Na^+ ions are distributed in the cage. By the loading of guest Na atom into sodalite, Na_4^{3+} cluster can be formed in the β-cage as shown in Fig. 1 (b). In the cluster, one unpaired s-electron provided by the guest Na atom is shared among four Na^+ ions and confined in the cage. When the clusters are formed in all the cages, antiferromagnetic (AFM) ordering appears below the Néel temperature of T_N = 48 K because of the exchange interaction between adjacent clusters via the window of the cage. The magnetic phase transition has been confirmed by susceptibility, ESR, NMR, μSR and so on, but there have been no reports on determining the magnetic structure. This might be due to the difficulties originated from the large unit cell and resultant low spin density. In the present study, we prepared approximately 2 grams of powder specimen of Na-loaded sodalite and performed ND experiments for the first time by utilizing the spectrometer PONTA at the JRR-3 at JAEA.

We succeeded in observing the 001 and 111 magnetic Bragg peaks at low temperature. The intensity was nearly three orders of magnitude weaker than that of the 011 nuclear Bragg peak. The temperature dependence of the intensity of 001 peak was well fitted by using a phenomenological equation of the order parameter with a three-dimensional Heisenberg antiferromagnet. The simultaneous observation of 001 and 111 magnetic Bragg peaks is consistent with the magnetic structure shown in Fig. 1 (c) where the electronic spin in the body center cluster and that in the corner cluster are antiparallel in the bcc lattice. We also evaluated the magnetic form factor from the ratio of the integrated intensities of the 001 and 111 magnetic Bragg peaks to the 011 nuclear one. The form factor is found to dump very quickly as a function of q as shown in Fig. 2. The simplest model describing the electron wave function of the cluster is a spherical well potential model with the diameter of the cluster. The dotted curve in Fig. 2 shows the calculated form factor of the 1s wave function confined in the spherical well with the inner diameter of 0.7 nm. The calculation results are in good agreement with the experimental ones. Therefore, it is evident that the s-electron responsible for the AFM order possesses a wave function delocalized over nanometer size in the cluster.

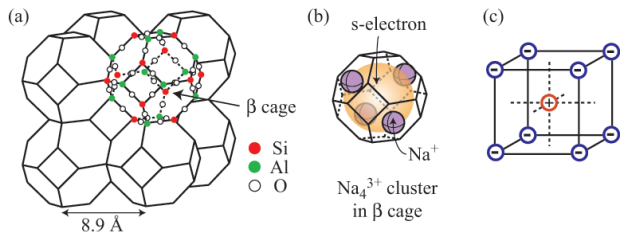

Fig. 1. Schematic illustrations of (a) crystal structure of aluminosilicate sodalite, (b) Na_4^{3+} cluster formed in the β-cage, and (c) magnetic structure model of Na clusters in sodalite. The framework of sodalite consists of Si, Al and O covalent-bonding network. The β-cages with an inner diameter of 0.7 nm are arrayed in a bcc structure. In the Na_4^{3+} cluster, one unpaired s-electron is shared among four Na^+ ions and confined in the β-cage. Under the antiferromagnetic ordered state, the electronic spin in the body center cluster and that in the corner cluster are coupled in antiparallel in the bcc lattice.

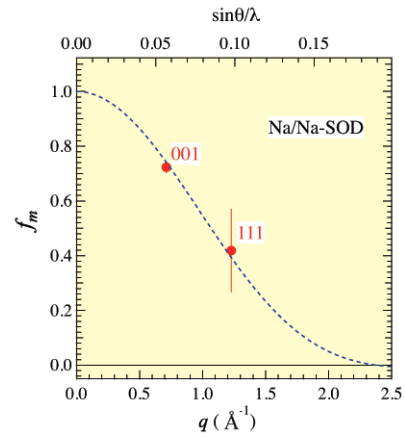

Fig. 2. Magnetic form factor of Na clusters in sodalite for scattering vector q. The closed circles show experimental results obtained by 001 and 111 magnetic Bragg peaks. The dotted curve shows the form factor evaluated from the 1s wave function in the spherical well potential with the inner diameter of 0.7 nm.

Reference
[1] T. Nakano, M. Matsuura, A. Hanazawa, K. Hirota, and Y. Nozue, Phys. Rev. Lett. **109**, 167208 (2012).

Authors
T. Nakano[a], M. Matsuura[a,b], A. Hanazawa[a], K. Hirota[a], and Y. Nozue[a]
[a]Osaka University
[b]Present Address: CROSS Tokai

Marked Change in the Ground State of $CeRu_2Al_{10}$ Induced by Small Amount of Rh Substitution

M. Sera, T. Nishioka, and K. Kindo

The recently discovered Kondo semiconductor CeT_2Al_{10} (T = Ru, Os, Fe) has attracted much attention because of their unusual ground states. Among many Kondo semiconductors, $CeRu_2Al_{10}$ and $CeOs_2Al_{10}$ are very rare systems exhibiting antiferromagnetic (AFM) order at T_0 ~ 30 K [1, 2]. As has been revealed by extensive studies up to now, the AFM ordered phases in these two compounds are strange. The AFM moment (M_{AF}) is parallel to the c-axis, which is not expected from the large anisotropy in magnetic susceptibility ($\chi_a > \chi_c > \chi_b$) in the paramagnetic region. Here, χ_a is the magnetic susceptibility along the a-axis, etc. The transition temperature is relatively high considering

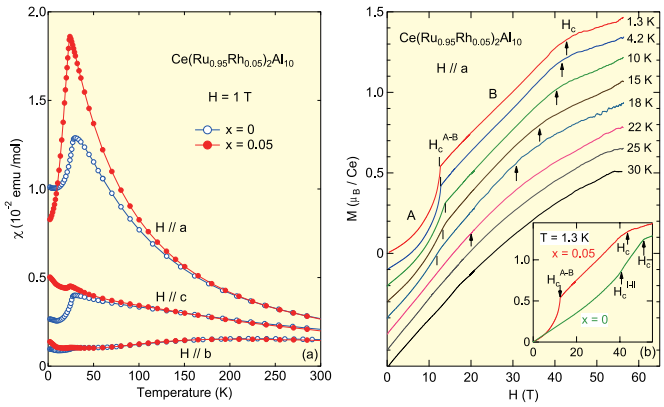

Fig. 1. (a) Temperature dependence of magnetic susceptibility of $Ce(Ru_{1-x}Rh_x)_2Al_{10}$ (x = 0, 0.05) along the a-, b-, and c-axes measured at 1 T. (b) Magnetization curve of $Ce(Ru_{0.95}Rh_{0.05})_2Al_{10}$ under various temperatures for H // a axis. The inset shows the M–H curve of $Ce(Ru_{1-x}Rh_x)_2Al_{10}$ (x = 0, 0.05) at T = 1.3 K for the H // a-axis.

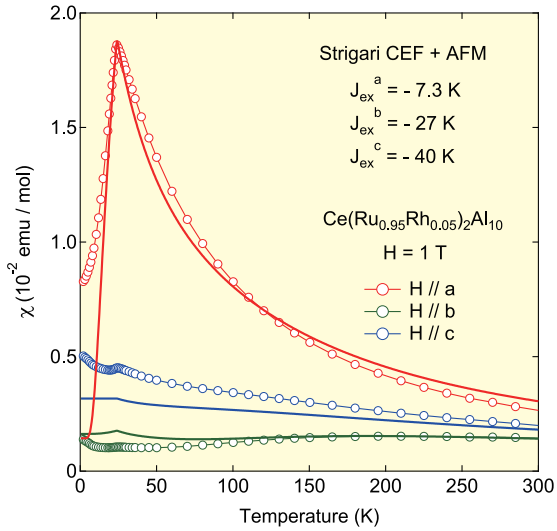

Fig. 2. Temperature dependence of magnetic susceptibility for H // a-, b-, and c-axes at 1 T calculated by mean field calculation using CEF level scheme obtained by Strigari *et al*. The solid lines represent the calculated results with the anisotropic exchange interaction of (J_a^{ex}, J_b^{ex}, J_c^{ex}) = (-7.3 K, -27 K, -40 K). The symbols are experimental results of $Ce(Ru_{0.95}Rh_{0.05})_2Al_{10}$.

the long distance (5.2 Å) between Ce ions. Although T_0 is high, the ordered moment is as small as 0.3 ~ 0.4μ_B/Ce. In our previous paper, we reported the high field magnetization curve of $CeRu_2Al_{10}$ and $CeOs_2Al_{10}$ for the magnetic field (H) along the a-axis, and proposed that the unusual AFM ordered phase in this system is caused by the large hybridization between the conduction band and the nearly localized 4f shell (c-f hybridization) along the a-axis, leading to the AFM order with M_{AF} // c [3].

Quite recently, Kobayashi *et al*. have reported the marked change in the magnetic susceptibility of $CeRu_2Al_{10}$ by Rh substitution [$Ce(Ru_{1-x}Rh_x)_2Al_{10}$, x = 0.1, 0.2, and 0.3]. They found in these compounds that, below ~ 150 K down to T_0, χ_a is strongly enhanced and shows a very large decrease with decreasing temperature after showing a sharp peak at T_0, and thus suggested a possible AFM order with M_{AF} // a. To clarify the origin of the marked change in the ground state by Rh substitution, we studied the magnetic susceptibility and high field magnetization of $Ce(Ru_{0.95}Rh_{0.05})_2Al_{10}$.

Figure 1(a) represents the temperature (T) dependence of χ of $Ce(Ru_{1-x}Rh_x)_2Al_{10}$ (x = 0, 0.05) along the a-, b-, and c-axes measured at 1 T. In $Ce(Ru_{0.95}Rh_{0.05})_2Al_{10}$, χ_a shows a large decrease with decreasing temperature after showing a sharp peak at T_0 ~ 24 K and the decrease in χ_c below T_0 observed in $CeRu_2Al_{10}$ originating from M_{AF} // c disappears by Rh substitution. These results suggest that the AFM order with M_{AF} // a occurs below T_0. In Fig. 1(b), we show the magnetization (M) curves of $Ce(Ru_{0.95}Rh_{0.05})_2Al_{10}$ under various temperatures for the H // a-axis. In $Ce(Ru_{0.95}Rh_{0.05})_2Al_{10}$, at 1.3 K, M exhibits a spin-flop transition at ~ 13 T. M at 50 T is ~ 1.4μ_B/Ce, which is larger than ~1.3μ_B/Ce for x = 0. This suggests a more localized nature of Ce ions in $Ce(Ru_{0.95}Rh_{0.05})_2Al_{10}$ than in $CeRu_2Al_{10}$. The experimental results were analyzed by mean field calculation for the two-sublattice model using the crystalline electric field (CEF) level scheme obtained by Strigari *et al*. and the anisotropic exchange interaction [4,5]. The calculated results of χ along the three crystal axes are shown in Fig. 2. χ_a in the paramagnetic region and a sharp peak at T_0 are reproduced well by the calculation. χ_c and χ_b, which are nearly independent of temperature, are also reproduced. On the basis of both experimental and calculated results, we conclude that, by a small amount of Rh substitution with one extra 4d electron, the large c-f hybridization along the a-axis, leading to the unusual ground state of $CeRu_2Al_{10}$, is markedly suppressed and the Ce ion in a Rh-substituted sample becomes close to the normal localized magnetic ion.

References

[1] T. Nishioka *et al*., J. Phys. Soc. Jpn. **78**, 123705 (2009).
[2] D. D. Khalyavin *et al*., Phys. Rev. B **82**, 100405 (2010).
[3] A. Kondo *et al*., Phys. Rev. B **83**, 180415 (2011).
[4] F. Strigari *et al*., Phys. Rev. B **86**, 081105 (2012).
[5] K. Kunimori *et al*., Phys. Rev. B **86**, 245106 (2012).

Authors

A. Kondo, K. Kindo, K. Kunimori[a], H. Nohara[a], H. Tanida[a], M. Sera[a], R. Kobayashi[b], T. Nishioka[c], and M. Matsumura[c]

[a]Hiroshima University
[b]Japan Atomic Energy Agency
[c]Kochi University

Gigantic Negative Magnetoresistance Effects in Pyrochlore Iridates

K. Matsuhira, M. Tokunaga, and M. Wakeshima

Since the discovery of high-T_c superconductivity in cuprate materials, physical properties of 3d transition metal oxides have been extensively studied. In this class of materials, strong Coulomb interaction dominates the other

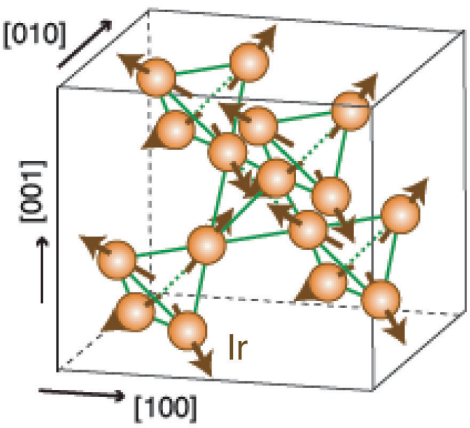

Fig. 1. Schematic illustration of the Ir-sites in the pyrochlore structure. Corner shared tetrahedra form three-dimensional network of the ions. The brown arrows represent the magnetic moments in the Ir ions.

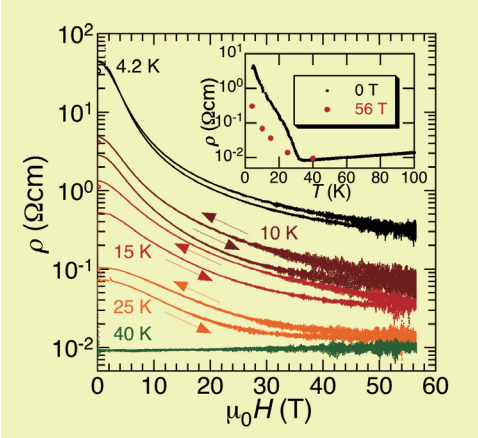

Fig. 2. Longitudinal magnetoresistance of a high-purity poly-crystal of $Nd_2Ir_2O_7$ [5]. The observed hysteresis can be caused by the change in temperature due to the magneto-caloric effect. Inset shows temperature dependence of the resistance at 0 T and 56 T.

interactions. Various interesting phenomena show up as a result of the interactions between charge carriers and local spins in the orbitals determined by the strong crystal electric fields. On the other hand, 5*d* transition metal oxides involve strong spin-orbit interaction, and hence, come to attract considerable attention as a playground for novel physics. In particular, rare-earth iridates $Ln_2Ir_2O_7$ (Ln: lanthanoid elements) are one of the attracting materials because of the geometrical frustration in the pyrochlore structure (Fig. 1).

The series of $Ln_2Ir_2O_7$ with *Ln* = Nd, Sm, Eu, Gd, Tb, Dy, and Ho exhibit metal-insulator transition when the Ir spins order at temperatures between 33 K and 141 K [1,2]; the Ir moments exhibit the antiferromagnetic ordering with q=0 (all-in/all-out state) shown in Fig. 1 [3,4]. Thereby, application of sufficiently high magnetic fields to remove the spin order is expected to induce insulator-metal transitions. We studied magnetoresistance on high-purity polycrystals of $Nd_2Ir_2O_7$ [5] in pulsed high magnetic fields up to 56 T. The results show prominent negative magnetoresistance effects below the metal-insulator transition temperature of 33 K (Fig. 2). The temperature dependence of the resistance at 56 T, however, remains semiconducting as shown in the inset of Fig. 2. This result suggests that the magnetic field of 56 T is insufficient to cause phase transitions in the Ir spin system. Similar behavior is observed when the *Ln* is magnetic, whereas non-magnetic Eu compound shows positive magnetoresistance effect [5]. Therefore, the observed negative magnetoresistance effects can be caused by the reduction of the spin fluctuation in the rare-earth ions and their coupling to the mobile 5*d* electrons via the *d-f* interactions.

References

[1] K. Mastuhira *et al*., J. Phys. Soc. Jpn. **76**, 043706 (2007).
[2] K. Mastuhira *et al*., J. Phys. Soc. Jpn. **80**, 094701 (2011).
[3] K. Tomiyasu *et al*., J. Phys. Soc. Jpn. **81**, 034709 (2012).
[4] H. Sagayama *et al*., Phys. Rev. B **87**, 100403(R) (2013).
[5] K. Mastuhira *et al*., J. Phys. Soc. Jpn. **82**, 023706 (2013).

Authors

K. Matsuhira, M. Tokunaga, M. Wakeshima, Y. Hinatsu, and S. Takagi

Cyclotron Resonance Studies in Ferromagnetic Semiconductors

G. A. Khodaparast and Y. H. Matsuda

The carrier-induced ferromagnetism in magnetic III-V semiconductors [1,2] has opened up several opportunities for device applications, as well as fundamental studies of a material system in which itinerant carriers interact with the localized spins of magnetic impurities. The origin of carrier-induced ferromagnetism is still controversial where reasonable agreement between theory and experiments has been noted for GaMnAs, but in contrast, the observation of T_c of 10 K for InMnAs films with carrier concentration of 10^{18}cm^{-3} is inconsistent with theory [3]. Based on theoretical calculations, InMnAs with a hole concentration of 10^{18}cm^{-3}should have a T_c of 8 K instead of the experimentally observed 40~90 K [2]. The case for MOVPE grown films is even more complex. Films with a carrier concentration of 10^{18}cm^{-3} have a T_c of 330 K and the T_c is nearly independent of carrier concentration [3]. In order to understand hole mediated ferromagnetism, probing the band structure in these materials are crucial. Cyclotron Resonance (CR) spectroscopy is an extremely powerful tool for the study of electronic states in semiconductors and here we present and compare the experimental and theoretical studies

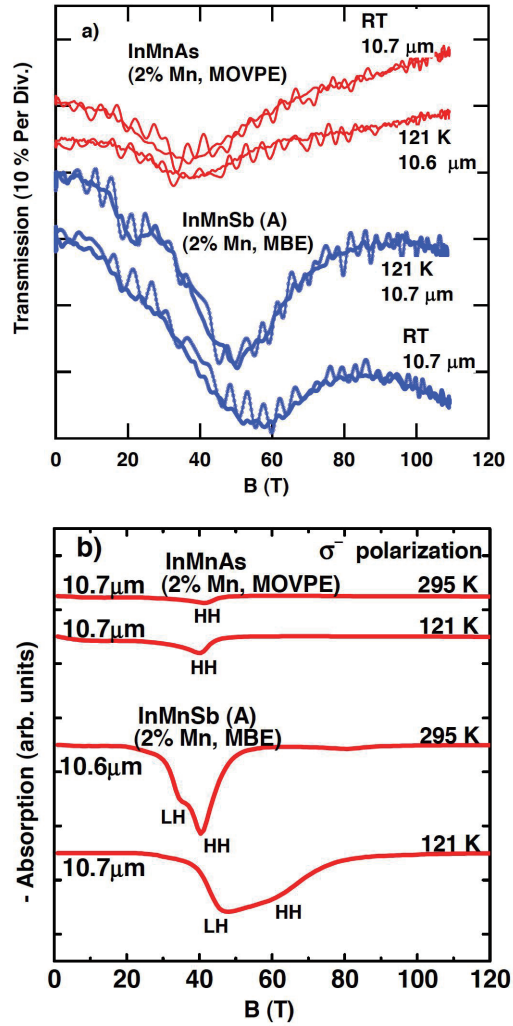

Fig. 1. a) CR spectra for InMnAs and InMnSb films. The CR of InMnSb at 295 K, was measured at 10.6 μm; whereas, the other three resonances were measured at 10.7 μm. b) Calculated CR spectra for InMnAs and InMnSb comparing to the experimental results in Fig.1a. The CR resonance in InMnAs originates from a single (HH only) transition; whereas, in InMnSb it arises from multiple (both LH and HH) transitions.

of the magneto-optical properties of p-type $In_{1-x}Mn_xAs$ and $In_{1-x}Mn_xSb$ ferromagnetic semiconductors films in ultrahigh magnetic fields oriented along [001].

Since these magnetic semiconductors usually have low carrier mobilities (typically of the order of 100 cm^2/Vs), a very high magnetic field is necessary to observe CR (i.e., $\omega_c\tau > 1$) where ω_c is the cyclotron frequency. Since CR directly provides the effective masses and scattering times of carriers, we can obtain detailed information on the itinerancy of the carriers while in transport measurements it is normally difficult to deduce the contributions of the mass and scattering time independently. In addition, our observations provide information on the band structure, sp-d exchange parameters (α, β), and the position of the Fermi level in these material systems. Recently in GaMnAs, the tunability of the Fermi level within the impurity band can be used to control the T_c.

CR measurements were performed using CO_2, H_2O, and CO lasers, providing laser radiation at 10.6, 10.7, and 16.9 and 5.53 μm. Magnetic fields exceeding 100 T were generated by a single turn coil technique. The external magnetic field was applied along the growth direction and measured by a pick-up coil around the sample, placed inside a continuous flow helium cryostat. Several IR wavelengths were used as the excitation source and the transmitted signal through the sample was collected using a fast liquid-nitrogen-cooled HgCdTe detector.

Figure 1a shows the results of the CR measurements for MBE grown InMnSb (sample A) and MOVOPE grown InMnAs with 2% Mn content. The observed cyclotron mass in the InMnSb(A) is larger than that in MOVPE grown InMnAs with similar Mn contents ($x \sim 0.02$). The larger hole density in the InMnSb compared to the InMnAs, can shift the Fermi energy to a much higher level. The cyclotron mass can be enhanced when the resonance transition takes place between the Landau levels with higher indices. The CR of the holes in InMnSb has been observed for the first time and in the case of Fig. 1a, the CR masses are $0.057m_0$ at room temperature (RT) and $0.051m_0$ at 121 K. These are much smaller than the band edge HH mass in InSb ($0.32m_0$). The cyclotron mobility, μ_{CR}, was extracted from the width of the resonance peaks. We have $\mu_{CR} = 4.8 \times 10^2$ $cm^2/(V\ s)$ at RT and $\mu_{CR} = 6.0 \times 10^2$ $cm^2/(V\ s)$ at 121 K. Lowering the temperature in InMnSb increased the mobility and reduced the effective mass, where the InMnAs resonance was not affected significantly by lowering the temperature. The CR absorption spectra shown in Fig.1b, is obtained from the calculated magneto-optical absorption due to transitions between different Landau levels. From Fermi's golden rule, the magneto-optical absorption coefficients at a given photon energy and for a magnetic field perpendicular to the sample can be calculated.

The observed effective mass in the InMnAs studied here is consistent with the heavy hole (HH) mass reported in an earlier CR study of *p*-type MBE grown InMnAs grown on GaAs [4] but different from the observation reported in InMnAs with the GaSb buffer layer [5]. The MOVPE grown InMnSb structure shows a much higher hole mobility and a factor of 100 less hole carrier density compared to the MBE grown structures.

References

[1] H. Munekata, H. Ohno, S. von Molnar, A. Segmuller, L. L. Chang, and L. Esaki, Phys. Rev. Lett. **63**, 1849 (1989).
[2] T. Schallenberg and H. Munekata, Appl. Phys. Lett. **89**, 042507 (2006).
[3] N. Rangaraju, Li Pengcheng, and B. W. Wessels, Phys. Rev. B **79**, 205209 (2009).
[4] Y. H. Matsuda, G. A. Khodaparast, M. A. Zudov, J. Kono, Y. Sun, F. V. Kyrychenko, G. D. Sanders, C. J. Stanton, N. Miura, S. Ikeda, Y. Hashimoto, S. Katsumoto, and H. Munekata, Phys. Rev. B **70**, 195211 (2004).
[5] G.A. Khodaparast, J. Kono , Y. H. Matsuda, S. Ikeda , N. Miura, Y. J. Wang, T. Slupinski, A. Oiwa, H. Munekata, Y. Sun, F. V. Kyrychenko, G. D. Sanders, and C. J. Stanton, Physica E **21**, 978 (2004).

Authors

G. A. Khodaparast[a], Y. H. Matsuda, T. R. Merritt[a], H. Saito, S. Takeyama, D. Saha[b], G. D. Sanders[b], C. J. Stanton[b], C. Feeser[c], B. Wessels[c], X. Liu[d], and J. Furdyna[d]
[a]Virginia Tech
[b]Department of Physics, University of Florida
[c]Northwestern University
[d]University of Notre Dame

Pulsed Laser Ablation in Supercritical CO_2 for Nanomaterials Synthesis

T. Kato, K. Terashima, and M. Baba

Pulsed laser ablation (PLA) is a versatile technique that allows the fabrication of high-quality thin films in vacuum, and it has also been increasingly used in liquids for the formation and functionalization of nanomaterials. Compared to gases and liquids, PLA in supercritical fluids (SCFs) offers further advantages for materials synthesis because of the favorable thermophysical properties of SCFs. For instance, in SCFs, coagulation of nanomaterials can be avoided because of the possibility to tune the solubility of the synthesized materials. Furthermore, certain thermophysical properties of SCFs, for instance the density fluctuation F_D, which characterizes the inhomogeneity of the local molecular density, present a local maximum at the critical point.

We have applied PLA in supercritical xenon (scXe) and carbon dioxide ($scCO_2$) near their critical points to the synthesis of diamondoids, which are $C(sp^3)$-$C(sp^3)$ hybridized hydrogen-terminated molecules whose cage structures

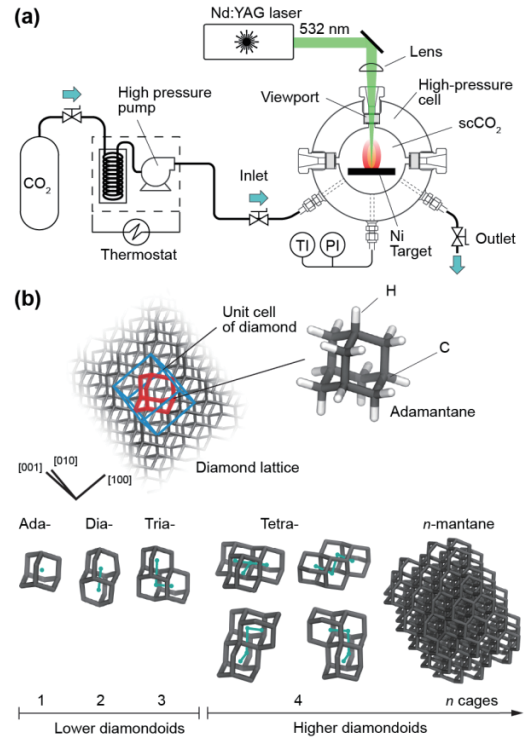

Fig. 1. (a) Schematic of pulsed laser ablation (PLA) in supercritical carbon dioxide ($scCO_2$). (b) Relation of diamondoids and diamond lattice and molecular structures of lower and higher diamondoids.

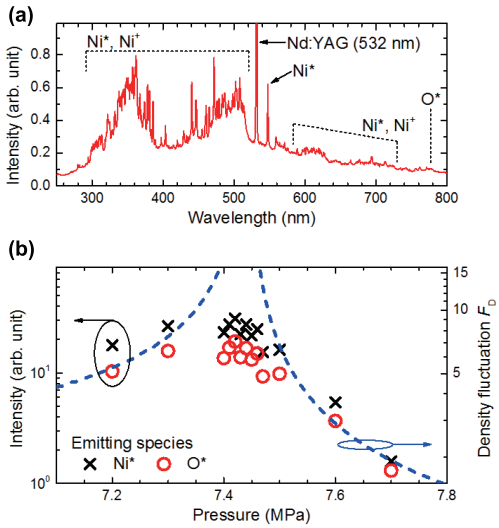

Fig. 2. (a) Optical emission spectrum acquired from PLA in $scCO_2$ near the critical point (b) Variation of emission intensities of Ni* and O* atomic lines and density fluctuation F_D of CO_2 fluid as a function of pressure. [4]

can be superimposed on a diamond lattice [1] (Fig. 1). Despite their promising physical properties and potential for a wide range of applications, the availability of high-order diamondoids is still very limited [2]. Using the first diamond member, adamantane, as a precursor and seed, we succeeded in the synthesis of higher diamondoids that had not been synthesized before, utilizing the dense and highly non-equilibrium reaction field of PLA plasmas in SCFs near the critical point [3].

Our joint group's study now aims to reveal the dynamics of the PLA reaction fields generated in SCFs using spectroscopic diagnostic equipment in the Spectroscopy Section of the Materials Design and Characterization Laboratory, for further improvement of the nanomaterials synthesis. Optical emission spectroscopy (OES) gave us information of target- and solvent-originated excited species in the PLA reaction field. We found that the emission intensities of both Ni (target) and O atoms (originating from the CO_2 solvent) reached local maxima that could be correlated to the change of the density fluctuation F_D [4] (Fig. 2). This is the first report on the critical anomaly in PLA dynamics in the world. The local maxima of emission intensities are probably due to the enhancement of the plasma excitation and effective quenching resulting from the large F_D, and it also means that the large number of excited species can contribute to the nanomaterials synthesis near the critical point. These experimental approaches for investigating the PLA dynamics will strongly assist the optimization of PLA nanomaterials synthesis in SCFs.

References

[1] S. Nakahara, S. Stauss, H. Miyazoe, T. Shizuno, M. Suzuki, H. Kataoka, T. Sasaki, and K. Terashima, Appl. Phys. Express **3**, 096201 (2010).
[2] J. E. Dahl, S. C. Liu, and R. M. K. Carlson, Science **299**, 96 (2003).
[3] S. Nakahara, S. Stauss, T. Kato, T. Sasaki, and K. Terashima, J. Appl. Phys. **109**, 123304 (2011).
[4] T. Kato, S. Stauss, S. Kato, K. Urabe, M. Baba, T. Suemoto, and K. Terashima, Appl. Phys. Lett. **101**, 224103 (2012).

Authors

T. Kato[a], S. Stauss[a], S. Kato[a], S. Himeno[a], K. Urabe[a], K. Terashima[a], M. Baba, and T. Suemoto

[a]Department of Advanced Materials Science, The University of Tokyo

Development of a Hard Magnetic Ferrite Exhibiting a Gigantic Coercivity and High Frequency Millimeter Wave Rotation

A. Namai and S. Ohkoshi

Magnetic ferrites such as Fe_3O_4 and Fe_2O_3 are extensively used because they are inexpensive and chemically stable. However, due to their low magnetocrystalline anisotropies, the coercivity of magnetic ferrites is generally low. The development of magnetic ferrites with a large coercive field (H_c) is an important issue because this type of ferrite can be used in various advanced applications.

In this work, we prepared rhodium-substituted ε-Fe_2O_3, ε-$Rh_xFe_{2-x}O_3$ nanomagnets, by a nanoscale chemical synthesis using mesoporous silica as a template. The transmission electron microscope image indicates that the obtained sample is composed of nanoparticles with an average particle size of *ca.* 35 nm. The X-ray diffraction patterns confirmed that the crystal structure is orthorhombic with $Pna2_1$ space group (Fig. 1a). The magnetic hysteresis loops measured at room temperature show that the H_c value increased with rhodium substitution and ε-$Rh_{0.14}Fe_{1.86}O_3$ exhibits a huge H_c value of 27 kOe. Furthermore, as shown in Figure 1b, a crystallographically oriented ε-$Rh_{0.14}Fe_{1.86}O_3$ nanomagnet recorded an H_c value of 31 kOe, which is the largest value among metal-oxide-based magnets and is comparable to those of rare-earth magnets (H_c values of Sm-Co and Nd-Fe-B magnet are 30 kOe and 25 kOe, respectively). Such a gigantic H_c value is explained by the following reasons. The particle size in the present series should be sufficiently small to form a single magnetic domain. In addition, the results of the first-principles calculations indicate strong Fe–O hybridization causing a non-zero orbital angular momentum on the Fe ion, which induces a large magnetocrystalline anisotropy. Furthermore, Rh–O–Fe hybridization is observed around the Rh substituted site, which enhances the magnetocrystalline anisotropy through the contribution from the orbital angular momentum on Rh.

Insulating magnetic materials with high magnetic anisotropy is expected to show high-frequency zero-field ferromagnetic resonance (natural resonance). The electromagnetic

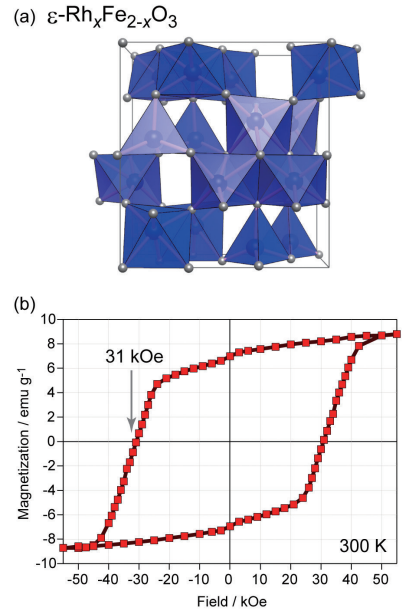

Fig. 1. (a) Crystal structure and (b) magnetic hysteresis of ε-$Rh_xFe_{2-x}O_3$.

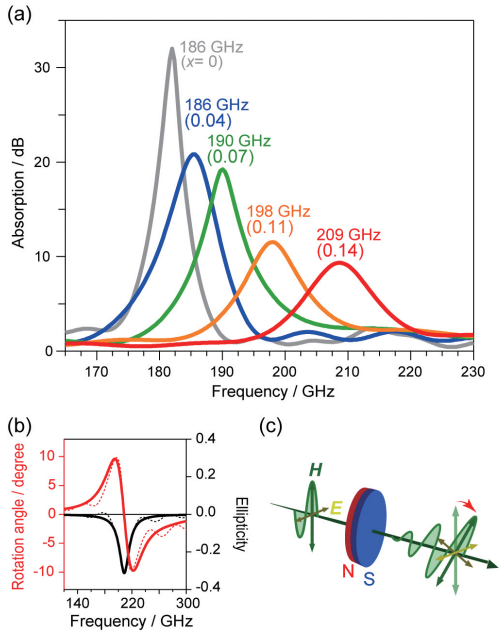

Fig. 2. (a) Electromagnetic wave absorption properties of ε-$Rh_xFe_{2-x}O_3$ measured by THz-TDS. (b) Rotation angle and ellipticity of the magnetized ε-$Rh_{0.14}Fe_{1.86}O_3$ pellet. (c) The schematic illustration of millimeter wave rotation.

wave absorption properties of ε-$Rh_xFe_{2-x}O_3$ were measured under zero-magnetic field at room temperature using terahertz time domain spectroscopy (THz-TDS). As shown in Figure 2a, resonance frequencies (f_r) were observed at 182 GHz (x = 0), 186 GHz (x = 0.04), 190 GHz (x = 0.07), 198 GHz (x = 0.11), and 209 GHz (x = 0.14). The observed f_r values are the highest among all magnetic materials. Furthermore, a magnetized ε-$Rh_{0.14}Fe_{1.86}O_3$ pellet sample exhibited magnetic rotation and ellipticity change of the propagated millimeter wave at 220 GHz, which is caused by gyromagnetic effect (Fig. 2b and 2c).

The gigantic H_c value has potential to be applied in future high-density magnetic recording media because the large H_c value enables the particle size to be greatly reduced while maintaining ferromagnetic properties. In addition, ε-$Rh_xFe_{2-x}O_3$ exhibits zero-field ferromagnetic resonance up to 209 GHz, and magnetic rotation of the propagated millimeter wave occurs due to an optically induced magnetic dipole transition at 220 GHz. The present material should be useful for high frequency millimeter wave absorbers and rotators (isolators or circulators) since it should restrict electromagnetic interference problems because the frequency of the magnetic rotation corresponds to the highest window of air (220 GHz band), which is the anticipated carrier frequency for next-generation millimeter wave wireless communications.

Reference
A. Namai, M. Yoshikiyo, K. Yamada, S. Sakurai, T. Goto, T. Yoshida, T. Miyazaki, M. Nakajima, T. Suemoto, H. Tokoro, and S. Ohkoshi, Nature Communications **3**, 1035 (2012). [*Nature Materials "Research Highlights" and Nature Japan "Focused Articles"*]

Authors
A. Namai, M. Yoshikiyo, K. Yamada, S. Sakurai, T. Goto[a], T. Yoshida[a], T. Miyazaki[a], M. Nakajima, T. Suemoto, H. Tokoro, and S. Ohkoshi
[a]Dowa Electronics Materials Co., Ltd.

Biexciton Luminescence from Individual Isoelectronic Traps in Nitrogen δ-Doped GaAs

K. Takamiya, H. Yaguchi, and H. Akiyama

Single photons and entangled photon pairs are expected to play an important role in the field of quantum information science and technology, such as quantum key distribution and quantum computation. Single isoelectronic traps formed by nitrogen–nitrogen (NN) pairs in GaAs are also promising candidates for generating single photons or entangled photon pairs [1-6]. The present paper reports on the observation of biexciton emission from individual isoelectronic traps in nitrogen δ-doped GaAs [7].

The sample used in this study was a nitrogen δ-doped GaAs layer grown on a semi-insulating undoped GaAs (110) substrate by low-pressure metalorganic vapor phase epitaxy. We measured micro-photoluminescence (PL) spectra at 4.2 K using a diode-pumped solid-state laser (λ=532nm) as the excitation source to observe the emission from single isoelectronic traps. The spatial and energy resolutions of the micro-PL measurement system used in this study were ~1 μm and ~30 μeV, respectively.

Figure 1 shows the excitation-power-dependent micro-PL spectra obtained from an individual isoelectronic trap in nitrogen δ-doped GaAs. As shown in this figure, sharp emission lines with full width at half maximum of about 30 μeV, which may be restricted by the energy resolution of the measurement system, are seen at 1.444 eV (labeled X) and 1.436eV (labeled XX). The PL line labeled X is assigned to the excitonic emission due to a NN pair named Z_2 because its photon energy is 1.444 eV. Figure 2 shows the intensity of the PL labeled X and XX as a function of laser power. The intensity of the excitonic emission labeled X increases linearly with increasing laser power while the PL intensity labeled XX clearly shows a quadratic dependence on the laser power under weak excitation conditions. This shows that the emission labeled XX is due to a radiative transition from a biexciton state to an exciton state.

In conclusion, we have observed biexciton luminescence from single isoelectronic traps formed by NN pairs in nitrogen δ-doped GaAs grown on GaAs(110). The biexciton binding energy was found to be 8 meV and almost always constant. Thus, biexciton emission with a highly reproducible photon energy can be easily obtained from single NN pairs in GaAs as in the case of exciton emission. Both the biexciton and exciton emission lines show random polariza-

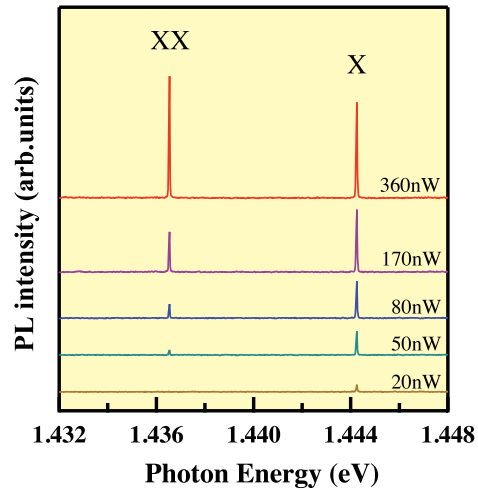

Fig. 1. Excitation-power-dependent micro-PL spectra obtained from an individual isoelectronic trap in nitrogen δ-doped GaAs.

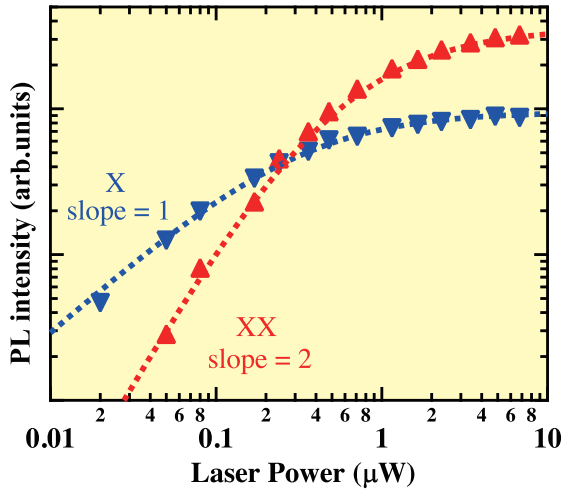

Fig. 2. PL intensity for the X and XX emission lines as a function of laser power.

tion and no fine-structure splitting, which shows promise for the application to polarization-entangled photon pairs.

References

[1] Y. Endo *et al*., J. Cryst. Growth **298** 73 (2007).
[2] Y. Endo *et al*., Physica E **40**, 2110 (2008).
[3] T. Fukushima *et al*., Physica E **42**, 2529 (2010).
[4] H. Yaguchi, Proc. SPIE **7945**, 79452F (2011).
[5] K. Takamiya *et al*., Mater. Sci. Forum **706**, 2916 (2012).
[6] M. Ikezawa *et al*., Appl. Phys. Lett. **100**, 042106 (2012).
[7] K. Takamiya *et al*., Appl. Phys. Express **5**, 111201 (2012).

Authors

K. Takamiya[a], T. Fukushima[a], S. Yagi[a], Y. Hijikata[a], T. Mochizuki, M. Yoshita, H. Akiyama, S. Kuboya[b], K. Onabe[b], R. Katayama[c], and H. Yaguchi[a]

[a]Saitama University
[b]Department of Advanced Materials Science, The University of Tokyo
[c]Tohoku University